

## Synthesis and Characterization ZnO-Fe<sub>2</sub>O<sub>3</sub> Nanocomposite with Thermal Plasma Method

Mohamad Reza Alikhani, Shahrooz Saviz\*, Amir Hossein Sari

Plasma Physics Research Center, Science and Research Branch, Islamic Azad University, Tehran, Iran

Received 29 October 2021; received in revised form 9 April 2022; accepted 18 April 2022 (DOI: [10.30495/IJC.2022.691319](https://doi.org/10.30495/IJC.2022.691319))

### ABSTRACT

In the present paper, a novel thermal plasma method is proposed to synthesize ZnO-Fe<sub>2</sub>O<sub>3</sub> nanocomposite, with different percentages of iron, namely 3, 5, and 7%. This method is an efficient feasibility of the ZnO-Fe<sub>2</sub>O<sub>3</sub> nanocomposite synthesis. The nanocomposites are synthesized by homemade direct current (DC) plasma torch. They are analyzed by different methods. The bandgap is determined by diffuse reflectance spectroscopy (DRS). The photocatalytic performance of ZnO-Fe<sub>2</sub>O<sub>3</sub> is evaluated. The results show that the structure of nanoparticles is spherical, which is more favored in the industry. Also, the particle size distribution is uniform. The average size of nanoparticle crystals increases with increasing iron content. Despite the formation of nanocomposites, due to the lack of support for nanoparticles, the results of photodegradation are not satisfactory.

**Keywords:** Thermal plasma, Plasma torch, Nanomaterial synthesis, Iron-doped ZnO, Photocatalysts

### 1. Introduction

Thermal plasma is generally produced by direct current (DC) or radio frequency (RF) plasma torches [1-5]. High enthalpy, high temperature and high speed are the main flame characteristics of these plasma torches [6-7]. The thermal plasma environment is ideal to facilitate rapid chemical reactions and high heat transfer for nanoparticle synthesis [8-11]. There are three main methods for producing nanoparticles using thermal plasma, which are: 1. The direct current transfer plasma torch, 2. The non-transferred direct current (DC) and 3. The radio frequency (RF) plasma torches methods.

In the first method, the target metal is selected as the anode and converted directly to nanoparticles by the transfer plasma arc. This process is not continuous due to the consumption of the anode and the need to replace it. The second and third methods are used for continuous production of nanoparticles. Through these methods, the desired particles with micron size enter the plasma turn into nanoparticles in a cooling chamber. One of flame in powder form. The powders evaporate and then the advantages of using thermal plasma method is the

spherical shape of the obtained nanoparticles [12-18]. Advantages of thermal plasma method: 1- it is a high temperature process, ceramic nanoparticles can also be synthesized, 2- Plasma is a powerful medium for accelerating chemical reactions, 3- Unlike the sol-gel method, this method does not require any coating agent, also high purity products are produced, 4- This method works at atmospheric pressure and high vacuum conditions are not required, 5- Compared to chemical methods, the synthesis time is very short, 6- It is possible to form very crystalline products, 7- The existing parameters for growth control, etc. of nanoparticles, are numerous.

Metal nanoparticles [19-20], non-metallic nanoparticles [21-25] and variety of composite nanomaterials [26-28] can be synthesized by thermal plasma method. At present, from an environmental point of view, the removal of toxic chemicals such as triphenylmethane dyes from waste waters of industries such as textiles, paper, leather, etc., is one of the most important environmental issues. There are several ways to remove these toxic dye contaminants, which have significant disadvantages. One of the most effective methods is the oxidation of organic pollutants, which is achieved when a strong oxidizing agent such as OH is produced. The advanced oxidation process, (AOP) is performed in

\*Corresponding author:

E-mail address: [shahrooz.saviz@srbiau.ac.ir](mailto:shahrooz.saviz@srbiau.ac.ir)

(S. Saviz)

different ways. The semiconductor mediated photo catalysis is one of the important AOPs. This type of AOPs has the capability of organic and inorganic pollutants removal. In contrast to other methods, in this method there are no harmful byproducts. If photocatalysts are present in an aqueous medium, and are exposed to ultraviolet photons, excited electrons moving from the charge layer to the conduction layer can produce hydroxyl radicals. The results of studies have shown that pairing different semiconductors and supporting them can lead to better results.

In addition to the unique and many applications such as piezoelectric, semiconducting and catalytic activity and the wide range of applications in sensors, solar cells, optoelectronics, and transducers in medical sciences, the ZnO is one of the popular photocatalysts due to its low price. However, its high bandwidth has led to poor photon absorption, resulting in reduced photocatalytic properties. To solve this problem, there are various methods that can be cited as follows: increasing the specific surface area by producing zinc nanoparticles, coupling with metallic and non-metallic elements to increase electrons and holes, and reducing bandwidth [29-56]. Nezamzadeh-Ejhi et al. [42], investigated the effect of supporting and hybridizing of FeO and ZnO semiconductors onto Iranian clinoptilolite nanoparticles and the effect of ZnO/FeO ratio in the solar photodegradation of fish ponds waste water. The results showed that the best light degradation is achieved when the ZnO photocatalyst is combined with a certain percentage of FeO. They also showed that the supported photocatalysts have far higher optical degradation properties. Also, in a certain gram/liter of photocatalyst, the optimum amount of light degradation is obtained, and in higher and lower amounts, this property is reduced.

In the present paper, the novel dc thermal-plasma method is used to synthesize iron-doped ZnO composite nanomaterials [57-59]. The rest of the paper is organized as follows: In Section 2, the used materials and the nanomaterial synthesis method are shown. Section 3 shows the used analyzes. The results and discussions are given in section 4. The most important results are given in section 5.

## 2. Experimental

### 2.1 Materials

Zinc powder (purity: 99.9%, size: 62  $\mu\text{m}$ ) and iron powder (purity: 99.9%, size: 45  $\mu\text{m}$ ) are used as raw materials. Methylene blue (Neutron Pharmaceutical Co.) was used to prepare the dye solution. An 8W UV-C lamp (Philips) was used to irradiate the dye solution.

### 2.2. Synthesis of nanocomposite

In our research, the thermal plasma method is used to obtain synthesis of the nanoparticles. As shown in Fig. 1 the main parts are: 1- the direct current (DC) plasma torch system (including: electric power supply, cooling chiller, gas capsule, powder feeding system, etc.) and cooling chamber. The plasma torch power is 40 kW (current: 500 A and voltage: 80 V). In a plasma torch, an electric arc is generated between the tungsten cathode and copper anode by the electric power supply. When plasma main gas (Argon) passes through this arc, it ionizes and due to high temperature and pressure, it leaves the plasma torch nozzle in the form of the flame. The temperature of this flame can be change from 4000  $^{\circ}\text{C}$  to 15000  $^{\circ}\text{C}$ . Argon flow rate is 20 LPM.

We prepared three mixtures of zinc powder and iron with different weight ratios as follows: Sample 1: 100g of Zn-2.5wt%Fe contain 2.5g of Iron and 97.5g of Zinc. Sample 2: 100g of Zn-4.3wt%Fe contain 4.3g of Iron and 95.7g of Zinc. Sample 3: 100g of Zn-6.1wt%Fe contain 6.1g of Iron and 93.9g of Zinc. After weighing the powders, the raw materials are manually mixed in a cylindrical vessel for 12 min and then injected into the powder feeder tank. The powder feeder system uses a vibrating mechanism to move the powders into the tube, through which the oxygen gas passes. The powder enters the plasma torch by the 15 lit/min oxygen carrier gas. Oxygen is selected because it assists in the complete oxidation process.

As shown in **Fig. 1**, the powders are guided into the nozzle by a copper tube. As soon as the powder particles enter the plasma flame, they are evaporated and atomized, and oxidized due to the presence of oxygen. Atoms can stick together to form larger particles in a short time. Particle size and geometry depend on the cooling rate. The faster the cooling, the smaller the size of the nanoparticles formed. The powder particles evaporate inside the plasma torch and cool down and get oxidized inside the cooling chamber, and the final nanoparticles accumulate on the wall of the cooling chamber. The temperature of the cooling chamber wall is maintained at 7  $^{\circ}\text{C}$ , by a chiller during the test. Test conditions are given in **Table 1**.

### 2.3. Characterization of iron-doped zinc oxide nanoparticle composites

The microstructure of the synthesized particles is observed, under a field-emission electron microscope (FE-SEM, MIRA3 TESCAN-XMU). The energy gap of the synthesized nanocomposites is calculated by diffuse reflectance spectroscopy (Avaspec 2048, Tech Avalight DHS).

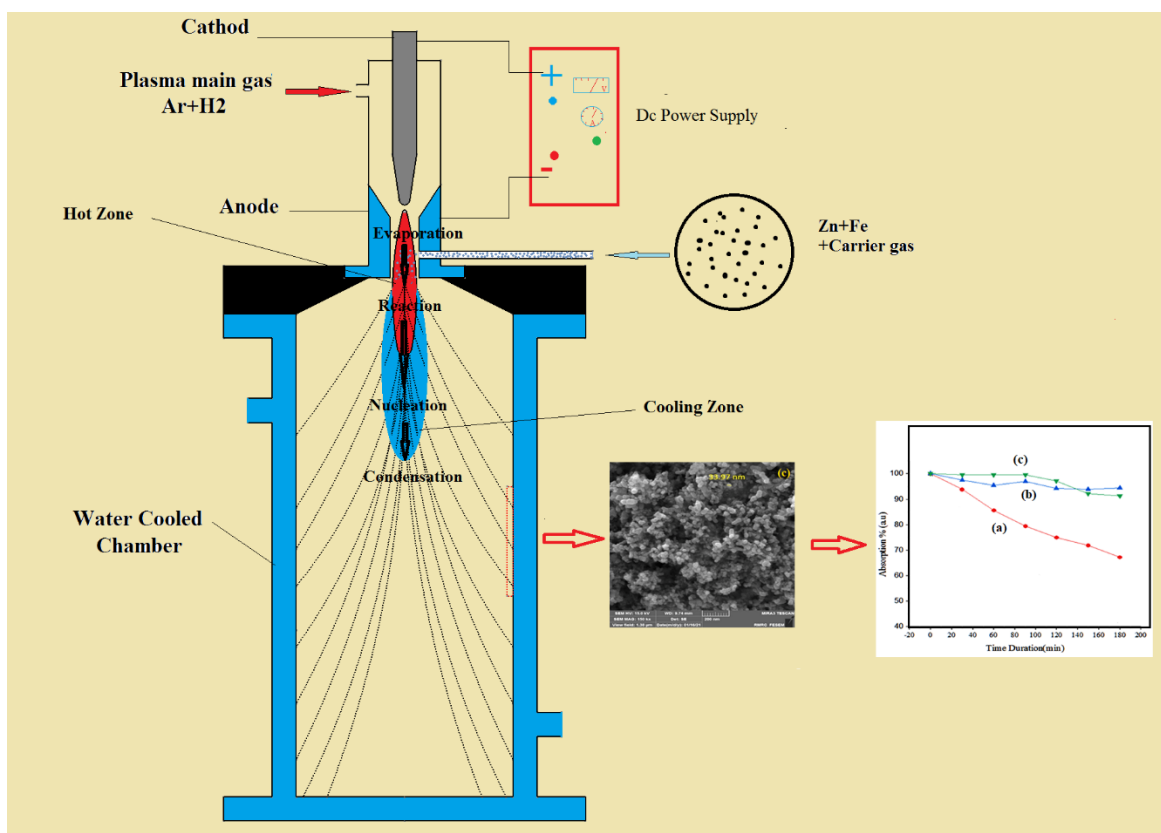


**Fig. 1.** Graphical abstract of the experiment

**Table 1.** Test conditions in the synthesis of iron-doped zinc oxide

Sample name	Sample 1	Sample 2	Sample 3	Sample 4
Fe wt%	0	2.5	4.3	6.1
Cooling chamber wall Temperature (°C)	7	7	7	7
Powder Carrier gas	Oxygen	Oxygen	Oxygen	Oxygen
Plasma main gas	Argon	Argon	Argon	Argon

### 3. Results and Discussion

#### 3.1. Crystallography

The phase characteristics, and the size of the nanoparticles, are determined using X-ray analysis (PW1730, Philips, Netherlands) in the range of 10 to 80° with a step size of 0.05° time per step of 1 s, a copper X-ray lamp wavelength of 1.56540 Å, voltage of 40 kV, and a current of 30 mA.

The XRD analysis for the three samples listed in **Table 1** is shown in **Fig. 2**. In these X-ray diffraction patterns; standard patterns are used to detect the crystal phases of the synthesized samples. According to card number 01-

089-1397, provided by the Joint Committee on Powder Diffraction Standards (JCPDS), the XRD patterns and *hkl* diffraction planes of ZnO nanoparticles agreed with that of hexagonal zinc oxide crystallite phase. The diffraction peaks positioned at 2θ values and related *hkl*, are as follows: 31.737° (1 0 0), 34.379° (0 0 2), 36.215° (1 0 1), 47.484° (1 0 2), 56.536° (1 1 0), 62.777° (1 0 3), 66.304° (2 0 0), 67.868° (1 1 2), 69.009° (2 0 1), 72.465° (0 0 4), 76.867 (2 0 2), 81.270 (1 0 4) and 89.492 (2 0 3).

**Fig. 2** shows that according to card number 00-024-0081, the Fe<sub>2</sub>O<sub>3</sub> nanoparticles has a cubic crystal phase. The 2θ position and *hkl* planes related to Fe<sub>2</sub>O<sub>3</sub> are as follows: 15.004 (1 1 0), 18.392 (1 1 1), 21.239 (2 0 0), 23.836 (2 1 0), 26.111 (2 1 1), 30.273 (2 2 0), 32.173 (2 2 1), 35.598 (3 1 1), 37.281 (2 2 2), 38.784 (3 2 0), 40.416 (3 2 1), 43.473 (4 0 0), 48.652(4 2 0), 53.888 (4 2 2), 57.168(5 1 1), 59.599(5 2 0), 60.459(5 2 1), 62.728 (4 4 0), 65.186(5 3 0), 71.403(6 2 0), 74.679 (5 3 3), 75.374 (6 2 2), 79.472 (4 4 4), 87.297(6 4 2), 90.250 (7 3 1), 92.205 (6 5 0), 95.095 (8 0 0) and 97.063 (8 1 1).

To calculate the average size of nanocrystal, the Scherrer formula is used as below:

$$D = \frac{K\lambda}{\beta \cos\theta} \quad (1)$$

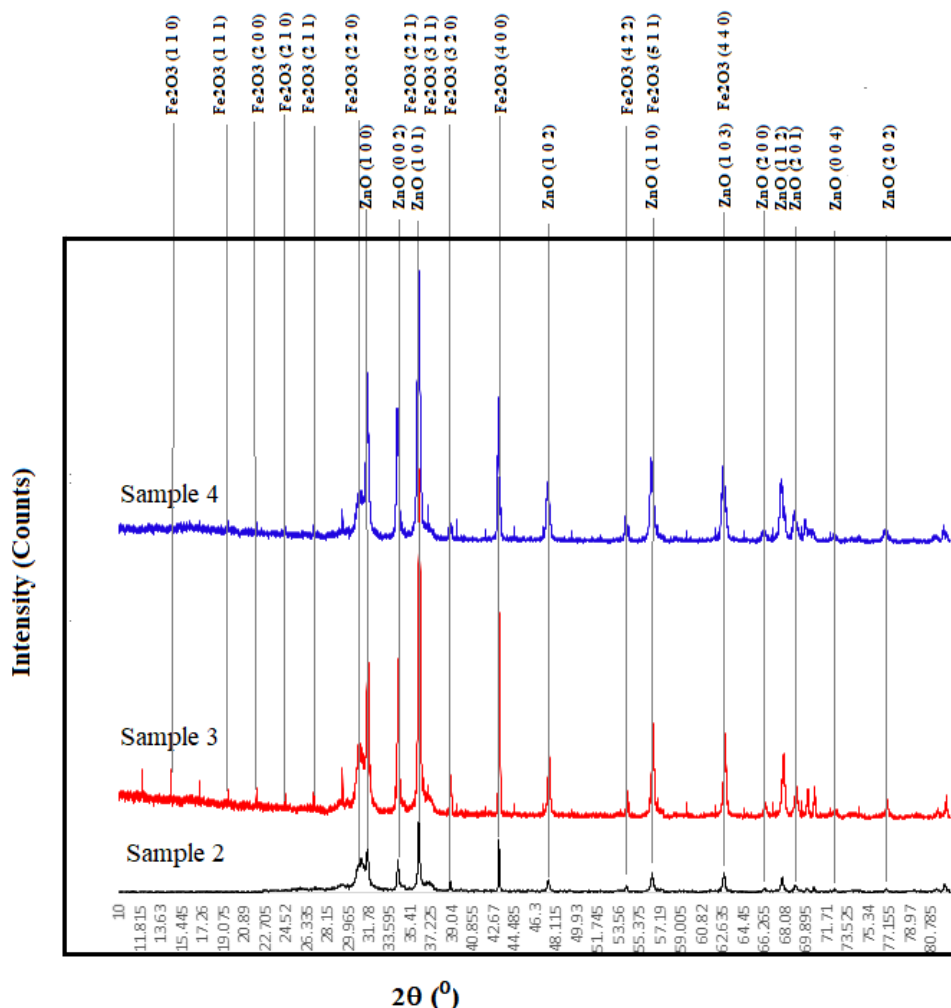


**Fig. 2.** XRD patterns of ZnO-Fe<sub>2</sub>O<sub>3</sub> nanocomposites for sample 2 (Zn-2.5wt%), sample 3 (Zn-4.3wt%Fe), sample 4 (Zn-6.1wt%Fe).

In Eq. 1, for cubic crystal structure,  $K = 0.94$ . Also,  $\lambda = 1.56540$ , Å is the wavelength of X-ray,  $\beta$  is the full width at half maximum intensity (FWHM) of the peak (in Rad) and  $D$  is the crystallite sizes (in nm).

Using Equation 1, the average size of the synthesized nanoparticles is obtained for three samples, which are shown in **Table 2**. As shown in **Table 2**, the average size of nanoparticle crystals increases with increasing iron content. The presence of peaks of single nanoparticles, ZnO and Fe<sub>2</sub>O<sub>3</sub>, indicates that the synthesis of ZnO-Fe<sub>2</sub>O<sub>3</sub> nanocomposite has been performed successfully. The XRD analysis of the  $\alpha$ -Fe<sub>2</sub>O<sub>3</sub> and ZnO nanoparticles (NPs) is performed by Nezamzadeh-Ejhi et al. [44-45]. They obtained the crystallite sizes by the Scherrer equation and by the Williamson-Hall equation for the ZnO,  $\alpha$ -Fe<sub>2</sub>O<sub>3</sub> and  $\alpha$ -Fe<sub>2</sub>O<sub>3</sub>-ZnO catalysts, respectively.

### 3.2. Nanoparticle morphology

The morphology of nanoparticles is studied by FESEM, and the results are presented in **Fig. 3**. All micrographs show the porous structure of the synthesized nanoparticles, resulting in an increase in the active surface area of the catalyst. This porous structure has also been observed in studies in which thermal plasma is used for the synthesis of nanoparticles [57-59]. Samples 1, 2, and 3 contain Fe atoms, and spherical nanoparticles with the average diameter of 30 nm formed.

EDX analysis for the three samples is shown in **Fig. 4**. As it transpires, the presence of zinc, iron and oxygen is evident. Also, considering the zinc and iron ratios of the three samples, it is evident that the peak intensity of zinc is much higher than that of iron.

**Table 2.** Average crystal size of the three samples, sample 1 (Zn-2.5wt%), sample 2 (Zn-4.3wt%Fe), sample 3 (Zn-6.1wt%Fe), with Scherrer formula.

Sample No.	$\theta^{\circ}$	FWHM(Rad)	crystallite sizes (nm)	average crystallite sizes (nm)
1	15.87	0.0165	9.17	17.9
	17.19	0.0035	43.9	
	18.1	0.0165	8.78	
	21.7	0.0165	9.67	
	15.87	0.0165	11.6	
2	17.19	0.0035	58	35.4
	21.7	0.0165	8.87	
	23.7	0.0165	63	
	15.87	0.0165	9.17	
	17.19	0.0017	90	
3	18.1	0.0165	9.2	46.1
	21.7	0.002	76	

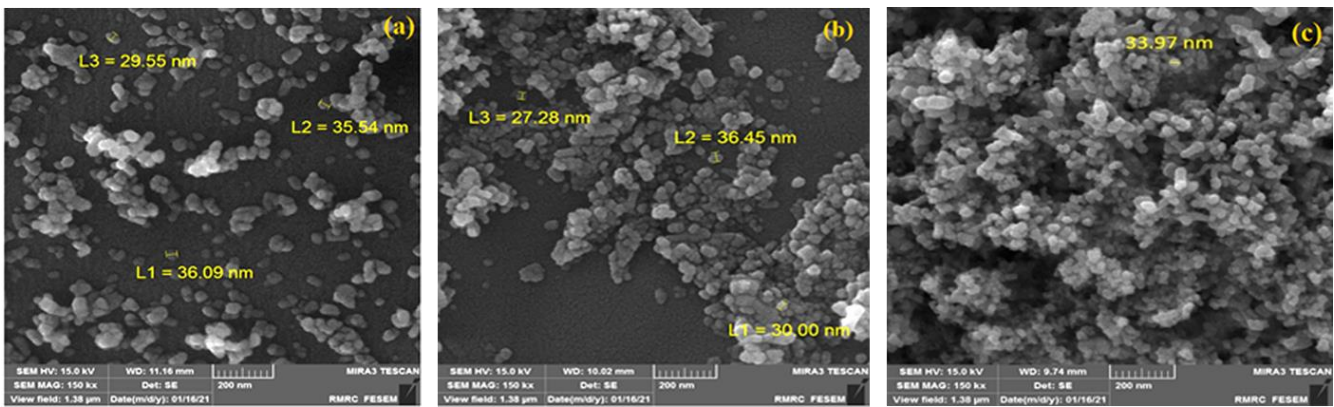


**Fig. 3.** SEM images of the nanocomposites (a) sample1(Zn-2.5wt%), (b) sample2 (Zn-4.3wt%Fe) and sample3 (Zn-6.1wt%Fe).

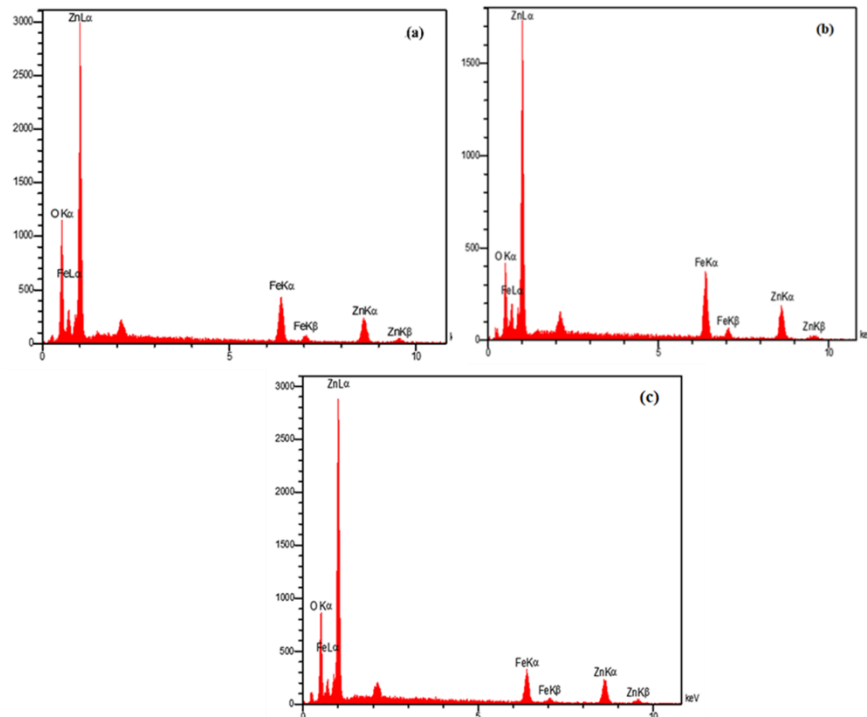


**Fig. 4.** EDX spectrum of the nanocomposites (a) sample1 (Zn-2.5wt%), sample2 (Zn-4.3wt%Fe) and sample3 (Zn-6.1wt%Fe).

3.3 Energy gap

The energy gap of the synthesized nanocomposites is calculated by DRS and the Kubelka-Munc equation [32-34]. **Fig. 5** shows the spectra obtained from the DRS analysis. The energy gap of samples 1, 2, and 3 is 3.14, 3.13 and 3.16 eV, respectively. With increasing impurity, when the valence bands of Fe atoms are placed beside Zn atoms, the resulting middle layers have a reduced energy gap. On the other hand, the significant increase of the grain size has a positive effect on the energy gap that makes it increase. The obtained values are the result of the combination of both effects.

### 3.4. Synthesized Nanocomposite Photocatalytic performance

In this section, the photodegradation properties of synthesized nanocomposites are examined. Synthesized nanocomposites are unsupported. Nezamzadeh-Ejhi et al. [42] showed that the photodegradation properties of ZnO, FeO and ZnOFeO in the non-supported state are much lower than in the NCP-supported state. The aim of this section is to show that if nanocomposites produced by plasma method, are not supported, they will not have very noticeable photodegradation properties. The aim in future articles will be to produce supported nanocomposites using the plasma method. The steps of testing the photocatalytic properties of the produced nanocomposites are as follows: 1-Dissolve 3 ppm of methylene blue powder in 100 ml of deionized water. This solution is prepared equally for the four synthesized samples. 2-Add 0.05 g of the synthesized nanocomposite to the prepared methylene blue solution. 3-The suspension was mixed by a magnetic stirrer for 30 min in the dark to establish an adsorption/desorption equilibrium between the powders and the dye. This is to eliminate the effect of surface adsorption on photocatalytic properties. 4-The solution is placed in a photoreactor for three hours. Inside the photoreactor, an 8-watt UVC lamp is used. Sampling every 30 minutes to measure the photo degradation. This is done with UV/Visible Spectrophotometer with wavelength range of 200 to 800 nm. 5-By collecting spectrometer data for four samples, Figure 5 is drawn.

**Fig. 6** shows that, as the percentage of iron increases, the rate of absorption increases. This means that the optical degradation property decreases with increasing iron content. Nezamzadeh-Ejhi et al. [44-45], considered the equal percentage of zinc and iron, and showed that the photodegradability of ZnO-Fe<sub>2</sub>O<sub>3</sub> nanocomposite is high.

When the iron content exceeds a certain amount, Fe atoms turn into a center for the recombination rather

than entrapment of the electron-hole pair for improving the photocatalytic activity. Iron can be found as Fe<sup>4+</sup>, Fe<sup>3+</sup>, and Fe<sup>2+</sup> in the crystalline lattice. Fe<sup>4+</sup> ions receive electrons under UV irradiation and are converted to Fe<sup>3+</sup> and subsequently Fe<sup>2+</sup> ions. In contrast, Fe<sup>2+</sup> ions receive the resulting holes and are converted into Fe<sup>4+</sup>. As a result, Fe atoms turn into centers for the recombination of the electron-hole pair, reducing the photocatalytic activity. Despite the lower photocatalytic activity of sample 1, it outperformed samples 2 and 3 with a dye removal efficiency of 33%. The dye absorption increased after 90 min for sample 2, which can be attributed to dye desorption from photocatalyst particles into the solution.

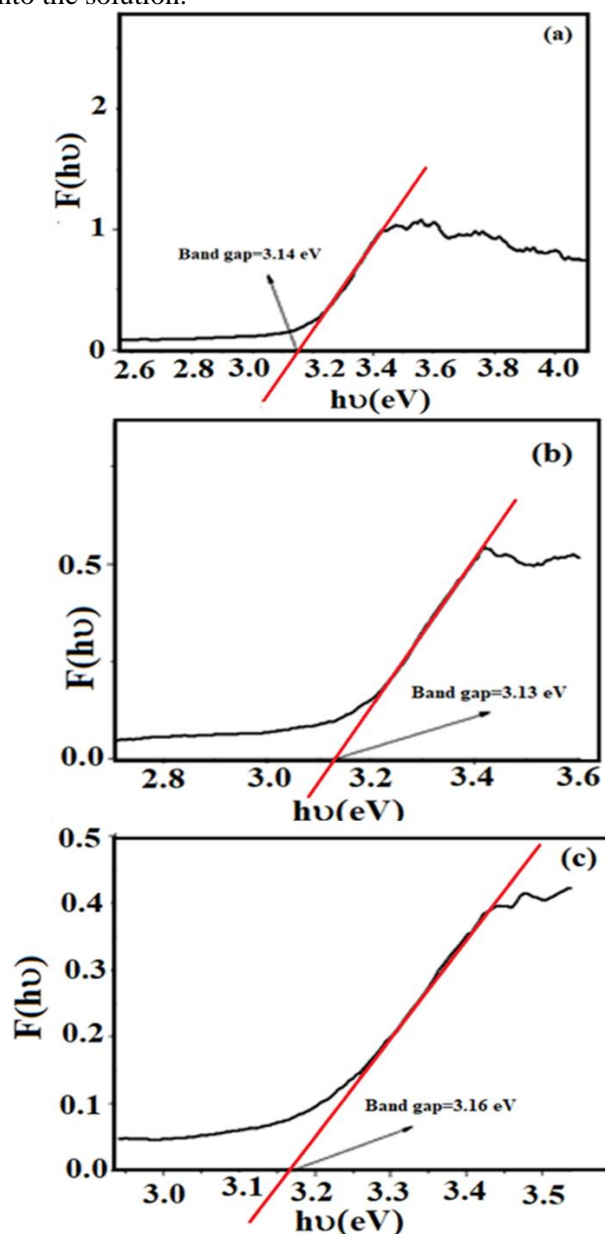


**Fig. 5.** DRS results of zinc oxide nanocomposites for (a) sample1 (Zn-2.5wt%), sample2 (Zn-4.3wt%Fe) and sample3 (Zn-6.1wt%Fe).

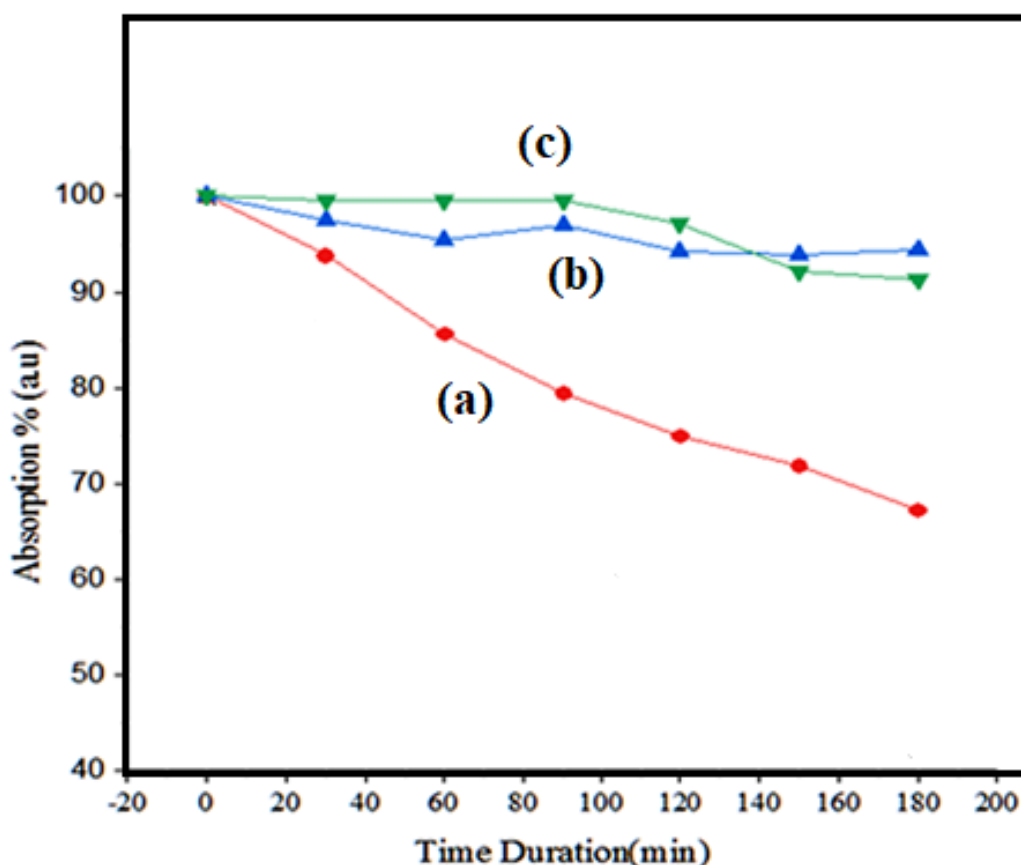


**Fig. 6.** Photocatalytic degradation of methylene blue for (a) sample1 (Zn-2.5wt%), (b) sample2 (Zn-4.3wt%Fe) and (c) sample3 (Zn-6.1wt%Fe).

#### 4. Conclusions

The most important results from this study are summarized as follows: 1-Synthesis of ZnO-Fe<sub>2</sub>O<sub>3</sub> composite nanoparticles by single stage thermal plasma technique. 2-The resulting nanocomposites have a spherical geometry. 3-Without the presence of support, the optical degradation properties are very weak. 4-The average size of nanoparticle crystals increases with increasing iron content.

#### Acknowledgements

Many thanks to Dr. Davoud Dorrnian for her help in analyzing the data.

#### References

- [1] M.I. Boulos, P. Fauchais, E. Pfender, Thermal plasmas : fundamentals and applications, (n.d.), first ed. Springer 2013.
- [2] E. Pfender, Plasma Process. 19 (1999) 1–31.
- [3] M. Gharaeinia, S. Saviz, A.H. Sari, J. Theor. Appl. Phys. 141 (2019) 1–10.
- [4] S. Khandanjou, M. Ghoranneviss, S. Saviz, Results in physics 7 (2017) 1440-1445.
- [5] S. Khandanjou, M. Ghoranneviss, S. Saviz, M.R. Afshar, Chinese Phys. B. 27 (2018) 028104.
- [6] M.I. Boulos, Pure Appl. Chem. 57 (1985) 1321–1352.
- [7] J. Heberlein, Pure Appl. Chem. 74 (2002) 327–335.
- [8] D. Vollath, J. Nanoparticle Res. 10 (2008) 39–57.
- [9] J. L. H. Chau, M.K. Hsu, C.C. Hsieh, and C.C. Kao, Mater. Lett. 59 (2005) 905-908.
- [10] G. Vissokov, I. Grancharov, T. Tsvetanov, Plasma Sci. Technol. 5 (2003) 2039.
- [11] M. Filkov, and A. Kolesnikov, Journal of Nanoscience (2016) 2016.
- [12] Lee, Y.I., Joung, J.W., Choi, J.R. and Lee, K.J., Samsung Electro Mechanics Co Ltd, U.S. Patent Application (2009) 12/081,274.
- [13] S. Ohno, J. Japan. Inst. Metals, 48 (1984) 640-646.
- [14] H. Bönemann, W. Brijoux, R. Brinkmann, R. Fretzen, T. Jousen, R. Köppler, B. Korall, P. Neiteler, and J. Richter, J. Mol. Catal. 86 (1994) 129-177.
- [15] Tadafumi Adschiri, and Yukiya Hakuta, K. Arai, Ind. Eng. Chem. Res. 39 (2000) 4901–4907.

- [16] S.H. Lee, S.M. Oh, D.W. Park, Mater. Sci. Eng. C. 27 (2007) 1286–1290.
- [17] S. Kumar, V. Selvarajan, P.V.A. Padmanabhan, K.P. Sreekumar, J. Mater. Process. Technol. 176 (2006) 87–94.
- [18] G. Masoumeh, S. Shahrooz, G. Mahmood, S.E. Ahmad, J. Theor. Appl. Phys. (2018) 122. 12 (2018) 85–91.
- [19] A.J. Shnoudeh, I. Hamad, R.W. Abdo, L. Qadumii, A.Y. Jaber, H.S. Surchi, and S.Z. Alkelany, In Biomaterials and bionanotechnology (2019) 527-612.
- [20] P. Buffat, J.-P. Borel, Phys. Rev. A. 13 (1976) 2287.
- [21] J.H. Seo, D.U. Kim, J.S. Nam, S.H. Hong, S.B. Sohn, S.M. Song, J. Am. Ceram. Soc. 90 (2007) 1717–1722.
- [22] D. Harbec, F. Gitzhofer, A., Powder Technol. 214 (2011) 356–364.
- [23] P. Buchner, H. Schubert, J. Uhlenbusch, M. Weiss, J. Therm. Spray Technol. 104 (2001) 666–672.
- [24] H. Nishiyama, M. Onodera, J. Igawa, T. Nakajima, JTST. 18 (2009) 593–599.
- [25] B. Bora, N. Aomoa, R.K. Bordoloi, D.N. Srivastava, H. Bhuyan, A.K. Das, M. Kakati, Curr. Appl. Phys. 12 (2012) 880–884.
- [26] Y.H. Hu, Catal. Today. 148 (2009) 206–211.
- [27] J.H. Seo, M.Y. Lee, J.S. Kim, Surf. Coatings Technol. 228 (2013) 91-96.
- [28] H. Zea, C.K. Chen, K. Lester, A. Phillips, A. Datye, I. Fonseca, J. Phillips, 89(1-2) (2004) 237-244.
- [29] V. Srikant, D.R. Clarke, J. Appl. Phys. 83 (1998) 5447-5451.
- [30] Z. Cao, Y. Wang, Z. Li, N. Yu, Nanoscale Res. Lett. 11 (2016) 1-6.
- [31] P. Sathishkumar, Z. Li, R. Govindan, R. Jayakumar, C. Wang, F. Long Gu, Appl. Surf. Sci. 536 (2021) 147741.
- [32] S. Gautam, H. Agrawal, M. Thakur, A. Akbari, H. Sharda, R. Kaur, M. Amini, J. Environ. Chem. Eng. 8 (2020) 103726.
- [33] I. Ahmad, M. Shoaib Akhtar, E. Ahmed, M. Ahmad, V. Keller, W. Qamar Khan, N.R. Khalid, Sep. Purif. Technol. 237 (2020) 116328.
- [34] K.E. Salem, A.M. Mokhtar, I. Soliman, M. Ramadan, B.S. Shaheen, N.K. Allam, Int. J. Hydrogen Energy. 46 (2021) 209-220.
- [35] N.A. Putri, V. Fauzia, S. Iwan, L. Roza, A.A. Umar, S. Budi, Appl. Surf. Sci. 439 (2018) 285-297.
- [36] T.S. Ko, S. Yang, H.C. Hsu, C.P. Chu, H.F. Lin, S.C. Liao, T.C. Lu, H.C. Kuo, W.F. Hsieh, S.C. Wang, Materials Science and Engineering: B, 134 (2006) 54–58.
- [37] H. Yoo, R. Mauchauffe, and S. Y. Moon, Current Appl. Physic. 25 (2021) 18-23.
- [38] L. Roza, V. Fauzia, M.Y.A. Rahman, I. Isnaeni, P.A. Putro, Opt. Mater. (Amst). 109 (2020) 110360.
- [39] H. Sudrajat, S. Babel, J. Water Process Eng. 16 (2017) 309–318.
- [40] B. Ghanbari Shohany, A. Khorsand Zak, Ceram. Int. 46 (2020) 5507-5520.
- [41] A. Nezamzadeh-Ejhieh, and E. Shahriari, J. Indust. Eng. Chem. 20 (2014) 2719-2726.
- [42] M. Bahrami, and A. Nezamzadeh-Ejhieh, Mater. Sci. Semicond. Proces. 27 (2014) 833-840.
- [43] B. Khodadadi, and M. Bordbar, Iran. J. Catal. 6 (2016) 37-42.
- [44] M. Bordbar, S. Forghani-Pilerood, and A. Yeganeh-Faal, Iran. J. Catal. 6(5) (2016) 415-421.
- [45] A. Noroozi, and A. Nezamzadeh-Ejhieh, Chem. Physic. Lett. 752 (2020) 137587.
- [46] A. Yousefi, and A. Nezamzadeh-Ejhieh, Iran. J. Catal. 11(3) (2021) 247-259.
- [47] M. Balakrishnan, and R. John, Iran. J. Catal. 10(1) (2020) 1-16.
- [48] H. Derikvandi, and A. Nezamzadeh-Ejhieh, J. Photochem. Photobio. A: Chem. 348 (2017) 68-78.
- [49] A. Sobhani-Nasab, M. Eghbali-Arani, S.M. Hosseinpour-Mashkani, F. Ahmadi, M. Rahimi-Nasrabadi, and V. Ameri, Iran. J. Catal. 10(2) (2020) 91-99.
- [50] S. Senobari, and A. Nezamzadeh-Ejhieh, Spectrochimica Acta Part A: Mol. Biomol. Spec. 196 (2018) 334-343.
- [51] A. Nezamzadeh-Ejhieh, and S. Hushmandrad, Appl. Catal. A: General 388(1-2) (2010) 149-159.
- [52] A. Nezamzadeh-Ejhieh, and M. Karimi-Shamsabadi, Appl. Catal. A: General 477 (2014) 83-92.
- [53] M. Karimi-Shamsabadi, and A. Nezamzadeh-Ejhieh, J. Mol. Catal. A: Chemical 418 (2016) 103-114.
- [54] M. Mehrali-Afjani, A. Nezamzadeh-Ejhieh, and H. Aghaei, Chem. Phys. Lett. 759 (2020) 137873.
- [55] S. Salmanderis, and A. Nezamzadeh-Ejhieh, Desali. Water Treat. 197 (2020) 200-212.
- [56] B. Manikandan, K.R. Murali, and R. John, Iran. J. Catal. 11(1) (2021) 1-11.
- [57] H.F. Lin, S.C. Liao, S.W. Hung, J. Photochem. Photobiol. A Chem. 174 (2005) 82–87.
- [58] M. Nirmala, A. Anukaliani, Mater. Lett. 65 (2011) 2645-2648.
- [59] S. T. Park, T. H. Kim, D. W. Park, App. Surf. Sci. 374 (2016) 257-264.